Prediction of steel nanohardness by using graph neural networks on surface polycrystallinity maps

Kamran Karimi[1],* Henri Salmenjoki[2], Katarzyna Mulewska[1], Lukasz Kurpaska[1], Anna Kosińska[1], Mikko J. Alava[1,2], and Stefanos Papanikolaou[1†]
[1] *NOMATEN Centre of Excellence, National Center for Nuclear Research, ul. A. Sołtana 7, 05-400 Swierk/Otwock, Poland*
[2] *Aalto University, Department of Applied Physics, PO Box 11000, 00076 Aalto, Espoo, Finland*

As a bulk mechanical property, nanoscale hardness in polycrystalline metals is strongly dependent on microstructural features that are believed to be heavily influenced from complex features of polycrystallinity —namely, individual grain orientations and neighboring grain properties. We train a graph neural network (GNN) model, with each grain center location being a graph node, to assess the predictability of micromechanical responses of nano-indented low-carbon 310S stainless steel (alloyed with Ni and Cr) surfaces, solely based on surface polycrystallinity, captured by electron backscatter diffraction maps. The grain size distribution ranges between $1 - 100$ μm, with mean grain size at 18 μm. The GNN model is trained on a set of nanomechanical load-displacement curves, obtained from nanoindentation tests and is subsequently used to make predictions of nano-hardness at various depths, with sole input being the grain locations and orientations. Model training is based on a sub-standard set of $\sim 10^2$ hardness measurements, leading to an overall satisfactory performance. We explore model performance and its dependence on various structural/topological grain-level descriptors, such as the grain size and number of nearest neighbors. Analogous GNN model frameworks may be utilized for quick, inexpensive hardness estimates, for guidance to detailed nanoindentation experiments, akin to cartography tool developments in the world exploration era.

I. INTRODUCTION

Polycrystals consist of complex crystalline grain networks that are known to dictate multiscale mechanical responses [1]. Nevertheless, inherent microstructure-property-process correlations may not be typically captured by constitutive relations and contain overwhelming complexity [2]. A remarkable exception is the famous Hall–Petch relationship [3, 4], connecting grain size and strength [5, 6]. Primary strengthening mechanisms, such as dislocation pile-ups and slip transfer capacity (across adjacent grains), are closely tied to intrinsic geometry of grains as well as their crystallographic orientation and associated degree of misalignment across boundaries [7–10]. Indeed, conventional phenomenological frameworks are limited in these respects, thus significantly restricting their predictive capacities [1]. In this paper, we construct a machine-learned graph neural network (GNN)-based framework from a fairly large ensemble of intrinsic structural features associated with the complex polycrystallinity of 310S steel. Using a relevant set of nano-mechanical tests, our supervised model is trained to produce interpretable predictions of micromechanical responses and indentation hardness solely based on (an appropriate suite of) microstructural predictors. The proposed framework may complement elaborate experimental and numerical investigations of metals' surface polycrystallinity by drastically improving material surface exploration for mechanical purposes.

Graph-based representations of polycrystals have been quite common in the attempt to describe microstructre-property relationships [11–14]. However, individual grain behaviors in polycrystals have been challenging to identify, with a wealth of constitutive parameters being commonly used to model them [14]. GNNs provide a way to capture and learn these behaviors in a consistent way, that can then be used to predict mechanical responses, solely based on the grain environment. GNNs combine conveniences of both conventional (feature-based) machine learning methods and deep learning, but with unstructured architectures that are more adherent to real physical contexts [15–18]. GNN has been used in recent applications in materials science relevant to dynamics of glassy systems [19, 20] as well as property predictions in crystalline materials [21] and some aspects of polycrystalline metals [22].

Nanoindentation tests provide valuable insights into complex microstructural strengthening and hardening mechanisms at the nanoscale, albeit with size effects [23] that mask bulk microstructural responses [24–26]. Electron microscopy has been shown to significantly assist the interpretation of nanoindentation results in a wealth of materials [27–29]. Here, we integrate nanoindentation data, informed by electron backscatter diffraction (EBSD) mapping, with a supervised data-driven approach based on the graph neural net model to infer micromechanical responses and grain-scale hardness from the surface polycrystallinity information (see Fig. 1). We construct and train the GNN using an EBSD orientation imaging map containing individual grains' orientations and neighboring grain properties which was supplemented by a micromechanical data set corresponding to a nanoindented low-carbon 310S stainless steel

* kamran.karimi@ncbj.gov.pl
† stefanos.papanikolaou@ncbj.gov.pl

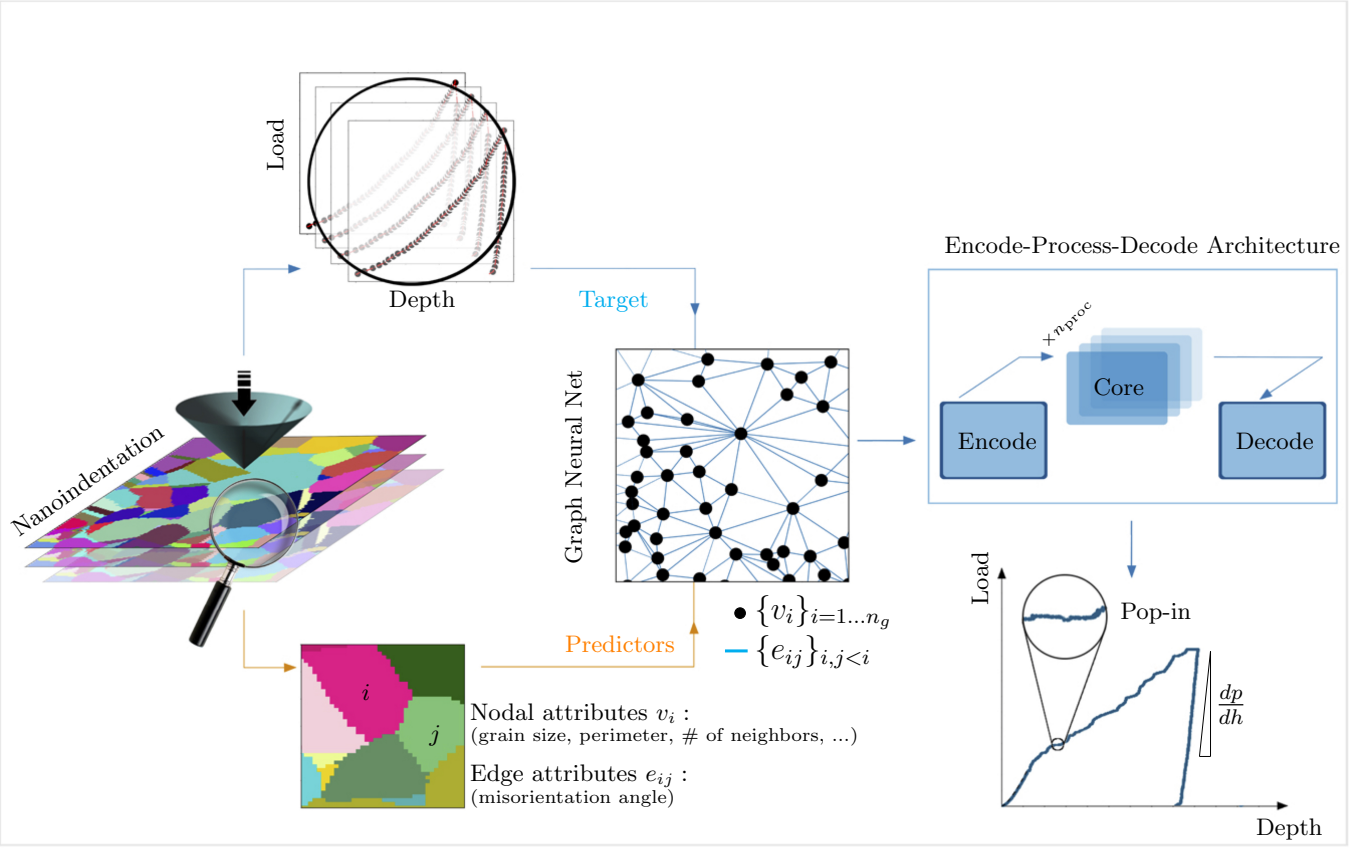

FIG. 1. The supervised machine-learning workflow combining nanoindentation and scanning electron microscope EBSD experimental data with graph neural net (GNN) based approach. The load-depth curves obtained from a nanoindented specimen serve as the *target* data for the GNN model. The grain microstructure and associated attributes are utilized as relevant *predictors*. The combined data set is employed to construct a GNN, with each grain center location being a graph node, to be trained through the "encode-process-decode" architecture. The model can learn from underlying correlations between the metallic microstructure and materials' mechanical response and make predictions on the latter (i.e. grain hardness) purely based on the former information.

(alloyed with Ni and Cr). The latter information consists of grain-scale load-displacement curves to be used as *response* variables for the prediction task. Microstructural *predictors* include an exhaustive list of (quantitative and categorical) grain-related characteristics with quite different scales that are all inferred and post-processed from the EBSD grain map (see Fig. 3). This includes grain size (`area`), `perimeter`, length of inner boundaries (`subBoundaryLength`), `diameter`, perimeter of a circle with the same area (`equivalentPerimeter`), perimeter divided by equivalent perimeter (`shapeFactor`), a boundary grain (`isBoundary`), a grain with inclusions (`hasHole`), an inclusion grain (`isInclusion`), and number of neighboring grains (`numNeighbors`) as well as the misorientation angle (`misOrientationAngle`) between neighboring grains and associated boundary length (`boundaryLength`). The grains' (numerical) descriptors are typically distributed over a broad range of scales with large variations in the associated nanomechanical response. The grain size distribution, as an example, has a lower cutoff at about 1 μm and mean value of 18 μm but is largely skewed with a long tail that extends up to 100 microns. Nevertheless, the overall predictive accuracy of our GNN model is fair given a relatively limited size of statistics (less than 200 sample points). This is verified in a systematic way by considering the learning process and its dependence on the training size as well as descriptor sets of varying size.

On top of high predictive accuracy, GNNs provide highly interpretable results and qualitative insights about underlying correlations between structural metrics and predicted nanomechanical response. More specifically, we find the grain diameter as a relevant hardness predictor which is in agreement with physics principles and could be verified in the context of the well-established Hall-Petch relationship, connecting the former and polycrystalline metals' strength (and/or hardness). In this framework, machine-learned models may accelerate experimental investigations relevant to the hardness *exploration* in polycrystalline metals. In addition to bulk mechanical properties (i.e. indentation hardness), our model may also be fine-tuned to accurately forecast indentation-

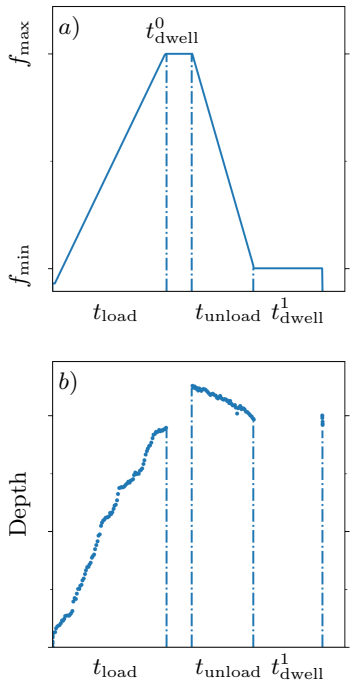

FIG. 2. Load-depth curves corresponding to the force-controlled nanoindentation tests. a) dynamics of the applied force b) measured indentation depths versus elapsed time. The graphs are not scale.

induced strain bursts (i.e. pop-ins) [30] and associated statistical distributions solely based on microstructural inputs.

II. METHODS

A. Nanoindentation Testing

The sample preparation, nanoindentation experiments, and microstructural characterization of the low-carbon 310S stainless steel but high in Ni ($19-22\%$) and Cr ($24-26\%$) content are detailed in [31]. We performed nanoindentation tests using the NanoTest Vantage system designed by Micro Materials Ltd. Hardness measurements were made at room temperature by using a Berkovich diamond indenter tip in a load-controlled manner at various depths. Dynamics of the applied force is given in Fig. 2(a) with the maximum load level, denoted by $f_{\max}$, exerted over the loading period of duration t_{load} and following (first) dwell period t^0_{dwell}. The specimen is subsequently unloaded to a residual force $f_{\min}$ over the time scale t_{unload} before it goes through the second dwell period of duration t^1_{dwell} for thermal drift corrections. The experiments were repeated over 12 distinct $f_{\max}$ values selected between $0.25-10$ mN and 15 different indentation points per $f_{\max}$ which were chosen to be about 20 μm (the mean grain size) apart in distance . This led to 180 mechanical tests in total. Here $f_{\min} = 0.25$ mN and $t^1_{\text{dwell}} = 60$ s. We also set $t_{\text{load}} = 10$ s, $t^0_{\text{dwell}} = 2$ s, $t_{\text{unload}} = 5$ s for $f_{\max} > 5$ mN and $t_{\text{load}} = 5$ s, $t^0_{\text{dwell}} = 1$ s, $t_{\text{unload}} = 3$ s otherwise. As the outputs, we measure indentation depths as a function of time with a temporal resolution of order $\Delta t \simeq 0.05$ s, as in Fig. 2(b).

B. Microstructural Characterization

The microstructural characterization and EBSD analysis of the indented sample was performed through a ThermoFisher Scientific Helios 5 UX scanning electron microscope equipped with an EDAX Velocity Pro EBSD system. The grain mapping was performed using a 20 keV electron beam with a 6.4 nA probe current. The EBSD map was subsequently reconstructed through an EDAX OIM Analysis 8 software by grouping sets of (at least 2) connected and similarly-oriented points (within $\pm 5^\circ$ uncertainties in angle) into individual grains. Crystallographic orientations, expressed in terms of Miller indices, can be assigned to each reconstructed grain (Fig. 3) to be used as model inputs for the GNN framework.

C. Training workflow

Nanoindentation load-depth curves were obtained from tests performed independently on $n_{\text{ind}} = 131$ individual grains (out of $n_g = 1080$ grains) based on a load-controlled protocol described above. We discretized the corresponding displacement and force data (excluding the second dwell period) as a function of time into regular arrays of size $n_{\text{dis}} = 100$, as in Fig. A1 and A2, and assembled the former in the target matrix $Y_{n_{\text{ind}} \times n_{\text{dis}}}$ to serve as training and test examples for our network. For the case of (large) grains with multiple indentation sites, we simply used the average displacement curves and our network was trained to predict deformation for individual grains. To reconstruct the network from the EBSD map (Fig. 3), each grain is treated as a separate node with index i and $i = 1...n_g$ in our graph. The graph connectivity is based on neighboring grains; that is, grain index i and j sharing a common border on the grain map are connected by an edge ij (see Fig. 1).

As a nodal *feature*, every node is assigned two dimensional Cartesian coordinates (`x,y`) associated with the center of each grain. Additional nodal attributes extracted from the original map (and expected to correlate with the mechanical response) include grain size (`area`), `perimeter`, length of inner boundaries (`subBoundaryLength`), `diameter`, perimeter of a circle with the same area (`equivalentPerimeter`), perimeter divided by equivalent perimeter (`shapeFactor`), a boundary grain (`isBoundary`), a grain with inclusions (`hasHole`), an inclusion grain (`isInclusion`), and number of neighboring grains (`numNeighbors`). The discretized force vector (as a control parameter in the ex-

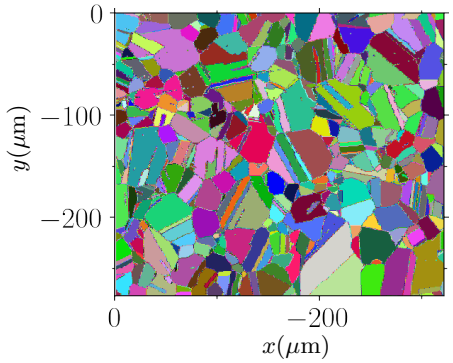

microstructural predictors	statistical mean	standard deviation
`x`	$-120.9(\mu m)$	75.5
`y`	$-148.1(\mu m)$	95.7
`area`	$82.9(\mu m^2)$	192.5
`perimeter`	$35.3(\mu m)$	48.5
`subBoundaryLength`	$0.1(\mu m)$	0.9
`diameter`	$11.0(\mu m)$	13.7
`equivalentPerimeter`	$20.1(\mu m)$	25.2
`shapeFactor`	1.5	0.5
`isBoundary`*	0.1	0.3
`hasHole`*	0.1	0.2
`isInclusion`*	0.2	0.4
`numNeighbors`	4.8	4.3
`misOrientationAngle`†	45.0°	12.1
`boundaryLength`†	7.3	10.9

* Binary variables
† Edge-based attributes

FIG. 3. The EBSD map used to extract numerical and binary microstructural variables as the model input.

periment) was concatenated with the above set of structural attributes of dimension $n_f = 12$ with the assembled feature matrix given as $X_{n_{\text{ind}} \times (n_{\text{dis}}+n_f)}$. To avoid features with significant variations in scale, every column of the above matrix was z-scored independently to have a zero mean and unit variance. Furthermore, the edges of the graph accommodate the misorientation angle (`misOrientationAngle`) between two neighboring grains i and j along with the associated boundary length (`boundaryLength`) as their features [32] .

The full set of nodal and edge-based features, i.e. $\{v_i\}_{i=1\ldots n_g}$ and $\{e_{ij}\}_{i,j<i}$ in the input graph, is initially encoded by an "Encoder" block and subsequently processed via a "Core" structure with $n_{\text{proc}} = 3$ rounds of processing based on the message-passing framework [15]. The "Decoder" block returns an output graph (with the exact same structure as the input one) based on the Core's outcome but with predicted attributes, i.e. expected displacements, based on the nodal and edge-based descriptors. Within the message-passing framework, the GNN applies two learning multilayer perceptrons (mlp) including an edge-based ϕ_e and node-based ϕ_v to each edge and node in order to compute updated node and edge attributes iteratively. The two mlp's have identical architectures and are composed of two hidden layers and eight neurons per layer with a tangent hyperbolic activation function.

The optimization of the GNN model was performed by minimizing the loss function based on the mean-squared error (MSE) between the actual displacements and those outputted by the GNN using the stochastic gradient descent over the entire parameter space with a learning rate of 10^{-3}. The graph data was split into training and testing sets and further trained using a four-fold cross validation. We note that both sets (the training and testing examples) are present within the same graph and that the node labels associated with the test data (i.e. displacements) are invisible during the training process. We use the GNNs library in Python which is DeepMind's implementation of graph neural nets based on Google's Tensorflow [15].

III. RESULTS

We first investigate the GNN model and assess its predictive power of nanoindentation responses based on the grains' surface structure and given history of applied forces. This includes a systematic analysis of the learning process of GNN from different subsets of existing grain-level predictors and varying training sizes. As a further validation, we extract grain nano hardness at various depths from the predicted response and quantify how well the predictions compare with the actual data.

A. Training and validation

The evolution of the GNN performance in minimizing the loss function is illustrated in Fig. 4(a) and (b). The learning rate corresponding to the training and test data are shown as a function of the number of iterations. The GNN training involves 92 training cases (70%) and 39 test observations (30%). Applying the GNN model to the training data set lead to a fairly low training set error (MSE < 10), showing a decay of at least four orders of magnitude after about 10^4 iterations. However, the test error rate appears to decrease more slowly as the optimization iterations proceed, decaying around two order of magnitude before it reaches a noise floor. Figure 4(c) and (d) show learning curves for the GNN-based prediction task, plots of MSE against the (relative) size of the training set. Here the results correspond to the four-fold cross-validation estimating the performance of the graph network over the training sets of varying sizes (and testing sets of a fixed size). The performance tends to improves as the (relative) training set size increases to 50%

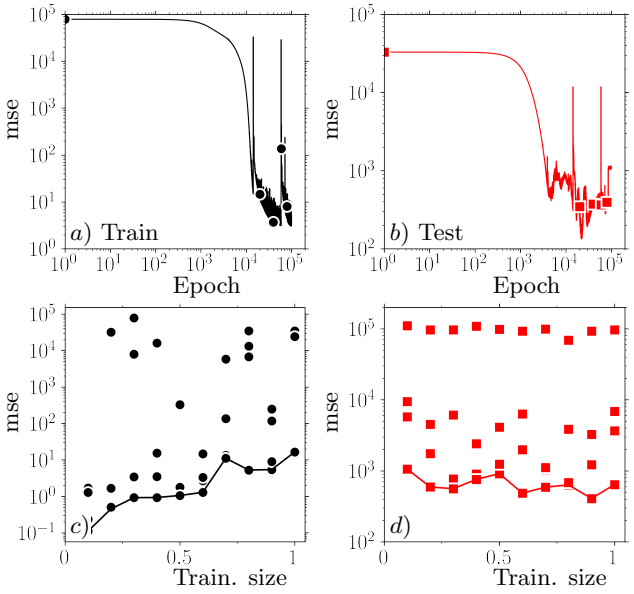

FIG. 4. Learning rate of the graph neural net corresponding to the a) training b) test set as a function of the number of iterations. Learning curves based on the cross-validated c) training and d) test mean squared errors for different training set sizes. The solid curves in c) and d) indicate lower bounds corresponding to the four-fold cross validation.

(less than 50 sample points) and increasing the number further leads to a small improvement.

The predictive power of GNN as a function of variable `area` is shown in Fig. 5 with the training and testing sets in Fig. 5(a) and Fig. 5(b). As expected, the latter displays larger variations in terms of the test errors (almost three orders of magnitude in MSE). The observed (anti-)correlations in both data sets indicate that, on average, the GNN exhibits a better performance with increasing grain size — cf. Fig. 5(c), Fig. 5(d), Fig. A1, and Fig. A2.

Figure 6 features the performance of the GNN model for all the predictor subsets (excluding the binary metrics). We pre-selected six quantitative variables including `area`, `perimeter`, `diameter`, `equivalentPerimeter`, `shapeFactor`, and `numNeighbors` to probe the training and test errors for every possible subset of size k = 1...5. In every analysis, the nodal coordinates (`x`, `y`) as well as the edge-based predictors `misOrientationAngle` and `boundaryLength` are incorporated as a fixed set of descriptors that are supplemented by additional variables as described above. Overall, the training errors in Fig. 6(a) and the associated base-line do not seem to be very sensitive to the subset size k. However, the minimum MSE corresponding to the testing set in Fig. 6(b) shows meaningful variations with k featuring a dip at $k = 4$ that corresponds to `perimeter`, `diameter`, `equivalentPerimeter`, and `numNeighbors` as predictor variables (see the table). In fact, the model performance will drastically degrade by including a subset of size $k = 5$. Out of the six numeric variables, `diameter` and `shapeFactor` are the most and least repeated entries of the table in Fig. 6 and, therefore, can be viewed as the most and least relevant descriptors.

B. Hardness Prediction

We infer grain-scale hardness from the GNN-predicted load-depth diagrams following the Oliver-Pharr framework [33]. The scatter plot of the predicted ($h_{\rm pred}$) and actual hardness ($h_{\rm act}$) is also shown in Fig. 7. The predictions associated with the testing set is, apart from a few outliers, reasonably distributed around $h_{\rm pred} = h_{\rm act}$. This is further quantified by a fairly high Pearson's correlation coefficient $\rho_h = \langle \hat{h}_{\rm pred}\ \hat{h}_{\rm act}\rangle$ with $\rho_h^{\rm test} \simeq 0.7$. Here $\hat{h} \doteq (h - \langle h\rangle)/{\rm var}^{\frac{1}{2}}(h)$ with the angular brackets $\langle . \rangle$ denoting an average. The hardness maps associated with the indented grains are shown for the actual and predicted data sets in in Fig. 8(a) and (b) as well as the difference between the former and the latter as in in Fig. 8(c). The actual map in Fig. 8(a) indicates that harder grains (in red) are, on average, smaller in size. We note that the bluish (reddish) colors in Fig. 8(c) indicate regions where the GNN tends to over(under)predict hardness. A visual inspection of Fig. 8(c) might indicate that grains with over(under)-predicted hardness may not possess any clear, distinguishable features (i.e. an abnormal geometry) that could delineate these cases. In this context, dimensionality reduction and/or clustering algorithms might allow for extracting anomalous attributes associated with such outliers (cf. Fig. 7) in a more systematic way.

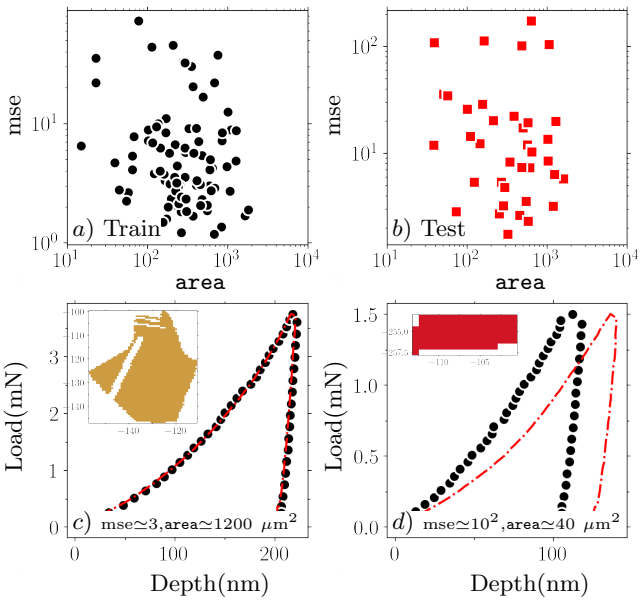

FIG. 5. a) Training and b) test errors plotted against `area`. Actual (symbols) and predicted (dashdotted curve) load-depth curves associated with a c) good and d) poor prediction within the test set. The insets show the corresponding grain maps.

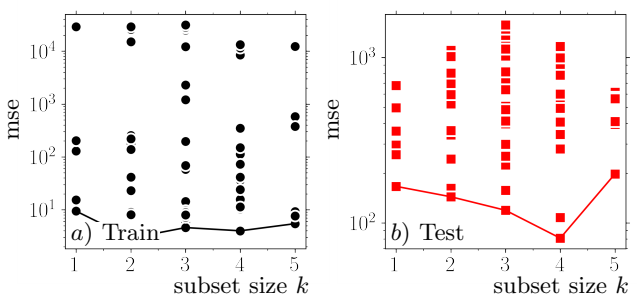

subset size k	1	2	3	4	5
`area`			†		†
`perimeter`			†	†	†
`diameter`	†		†	†	†
`equivalentPerimeter`		†		†	†
`shapeFactor`					†
`numNeighbors`		†		†	

FIG. 6. Validation curves determining a) training and b) test errors for varying sets of descriptors. Here symbols correspond to all possible subsets of size $k = 1...5$ corresponding to the full set of numeric variables `area`, `perimeter`, `diameter`, `equivalentPerimeter`, `shapeFactor`, `numNeighbors`. The solid curves indicate minimal errors corresponding to each k and the table denotes the associated set of predictors (relevant to the testing set) by †.

IV. CONCLUSIONS & DISCUSSIONS

We have studied the effectiveness and robustness of a GNN-based supervised machine learning model in predicting mechanical nanoindentation response from experimentally-measured grain microstructure replicated as a graph. Microstructural patterns are encapsulated in the GNN via a set of node-based and edge-based hidden layers that learn from nanoindentation-induced deformation in a supervised learning context. We have probed hardness as an experimentally measurable micromechanical property to test the predictive power of the GNN. A rich set of grain-level structural features was extracted from the grain map and the robustness and accuracy of the prediction task was verified with respect to varying subsets of selected descriptors.

Given the convenience of GNNs (i.e. predictiveness, speed, and interpretability) in the hardness prediction, the proposed framework may also be augmented to account for indentation-induced pop-in behavior abrupt displacement jumps (in a load-controlled indentation) and associated statistical distributions solely based on microstructural inputs. As pop-ins typically trigger as a result of the interplay between dislocations and embedding grain boundary, one might envision the use of more elaborate indicators of microstructure (such as dislocation density) to be incorporated as nodal and/or edge-based ingredients.

As a final remark, applications of data-driven methodologies shall not be regarded as substitutes but rather complements to laboratory-based measurements and/or high-throughput physics-based simulations. Machine-learned models require smooth access to well-maintained, accurate, and reusable data sets, relevant to materials' micro-structure and associated (micro-)mechanical response, which are otherwise impossible to measure in the absence of experimental/numeric observations. In fact, a coherent integration of the above methodologies will be essential in a way that they guide one another to achieve the desired speed, interpretability, and predictiveness of outcomes. Our GNN development provides a fine example in this context, where a fairly limited number of surface measurements (order 10^2 indentation tests) was performed for the prediction task. Nevertheless, the model outcomes will allow us to efficiently infer a *full* hardness cartography map from the prescribed force dynamics, as in Fig. 2(a), and a fine-scale EBSD analysis of nearly 10^3 grains.

ACKNOWLEDGMENTS

This research was funded by the European Union Horizon 2020 research and innovation program under grant agreement no. 857470 and from the European Regional Development Fund via Foundation for Polish Science International Research Agenda PLUS program grant no. MAB PLUS/2018/8. We wish to acknowledge fruitful discussions with Daniel Cieslinski.

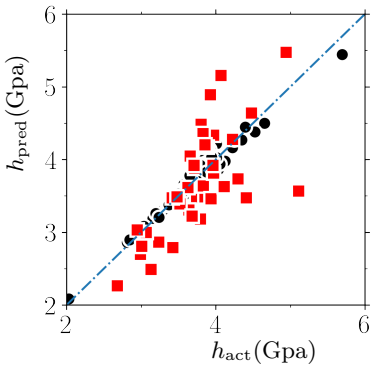

FIG. 7. Scatter plot of the predicted hardness and the actual values corresponding to the training set (●) and the test set (■). The diagonal dashdotted line indicates $h_{\rm pred} = h_{\rm act}$. The hardness is measured in Gpa.

[1] A. S. Wadhwa and H. S. Dhaliwal, *A Textbook of Engineering Material and Metallurgy* (Firewall Media, 2008).

[2] A. Lasalmonie and J. Strudel, Influence of grain size on

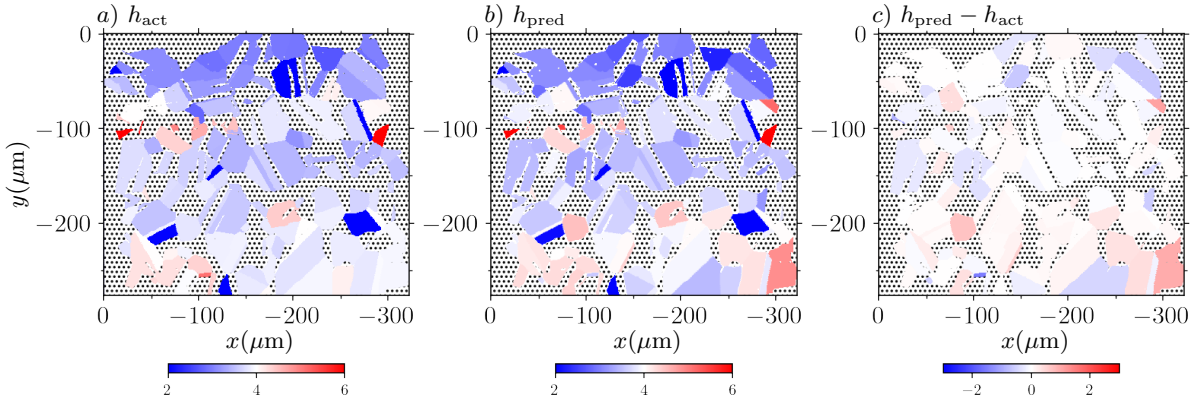

FIG. 8. Hardness maps (including indented grains only) associated with the a) actual data h_{act} b) GNN prediction h_{pred} c) difference between predicted and actual data $h_{\mathrm{pred}} - H_{\mathrm{act}}$. The harness is measured in Gpa. The hatched areas denote non-indented grains.

the mechanical behaviour of some high strength materials, Journal of Materials Science **21**, 1837 (1986).

[3] E. Hall, The deformation and ageing of mild steel: Iii discussion of results, Proceedings of the Physical Society. Section B **64**, 747 (1951).

[4] N. Petch, The cleavage strength of polycrystals, Journal of the Iron and Steel institute **174**, 25 (1953).

[5] A. Alavudeen, N. Venkateshwaran, and J. W. Jappes, *A textbook of engineering materials and metallurgy* (Firewall Media, 2006).

[6] B. Yang and H. Vehoff, Grain size effects on the mechanical properties of nanonickel examined by nanoindentation, Materials Science and Engineering: A **400**, 467 (2005).

[7] M. Wang and A. Ngan, Indentation strain burst phenomenon induced by grain boundaries in niobium, Journal of materials research **19**, 2478 (2004).

[8] T. Britton, D. Randman, and A. Wilkinson, Nanoindentation study of slip transfer phenomenon at grain boundaries, Journal of Materials Research **24**, 607 (2009).

[9] S. Pathak, J. Michler, K. Wasmer, and S. R. Kalidindi, Studying grain boundary regions in polycrystalline materials using spherical nano-indentation and orientation imaging microscopy, Journal of Materials Science **47**, 815 (2012).

[10] T. Ohmura, K. Tsuzaki, and F. Yin, Nanoindentation-induced deformation behavior in the vicinity of single grain boundary of interstitial-free steel, Materials transactions **46**, 2026 (2005).

[11] T. Ozturk, C. Stein, R. Pokharel, C. Hefferan, H. Tucker, S. K. Jha, R. John, R. A. Lebensohn, P. Kenesei, R. M. Suter, and A. D. Rollett, Simulation domain size requirements for elastic response of 3d polycrystalline materials, Modelling and Simulation in Materials Science and Engineering **24** (2015).

[12] M. Jackson, M. Groeber, S. Donegan, and D. Dimiduk, Advancements to the digital representation environment for analysis of materials in 3-dimensions—dream. 3d, Microscopy and Microanalysis **25**, 176 (2019).

[13] C. A. Bronkhorst, S. Kalidindi, and L. Anand, Polycrystalline plasticity and the evolution of crystallographic texture in fcc metals, Philosophical Transactions of the Royal Society of London. Series A: Physical and Engineering Sciences **341**, 443 (1992).

[14] C. A. Bronkhorst, J. R. Mayeur, V. Livescu, R. Pokharel, D. W. Brown, and G. T. Gray III, Structural representation of additively manufactured 316l austenitic stainless steel, International Journal of Plasticity **118**, 70 (2019).

[15] P. W. Battaglia, J. B. Hamrick, V. Bapst, A. Sanchez-Gonzalez, V. Zambaldi, M. Malinowski, A. Tacchetti, D. Raposo, A. Santoro, R. Faulkner, *et al.*, Relational inductive biases, deep learning, and graph networks, arXiv preprint arXiv:1806.01261 (2018).

[16] M. M. Bronstein, J. Bruna, Y. LeCun, A. Szlam, and P. Vandergheynst, Geometric deep learning: going beyond euclidean data, IEEE Signal Processing Magazine **34**, 18 (2017).

[17] J. Zhou, G. Cui, S. Hu, Z. Zhang, C. Yang, Z. Liu, L. Wang, C. Li, and M. Sun, Graph neural networks: A review of methods and applications, AI Open **1**, 57 (2020).

[18] K. Frydrych, K. Karimi, M. Pecelerowicz, R. Alvarez, F. J. Dominguez-Gutiérrez, F. Rovaris, and S. Papanikolaou, Materials informatics for mechanical deformation: A review of applications and challenges, Materials **14**, 5764 (2021).

[19] V. Bapst, T. Keck, A. Grabska-Barwińska, C. Donner, E. D. Cubuk, S. S. Schoenholz, A. Obika, A. W. Nelson, T. Back, D. Hassabis, *et al.*, Unveiling the predictive power of static structure in glassy systems, Nature Physics **16**, 448 (2020).

[20] H. Shiba, M. Hanai, T. Suzumura, and T. Shimokawabe, Unraveling intricate processes of glassy dynamics from static structure by machine learning relative motion, arXiv preprint arXiv:2206.14024 (2022).

[21] T. Xie and J. C. Grossman, Crystal graph convolutional neural networks for an accurate and interpretable prediction of material properties, Physical review letters **120**, 145301 (2018).

[22] D. C. Pagan, C. R. Pash, A. R. Benson, and M. P. Kasemer, Graph neural network modeling of grain-scale anisotropic elastic behavior using simulated and measured microscale data, arXiv preprint arXiv:2205.06324 (2022).

[23] W. D. Nix and H. Gao, Indentation size effects in crystalline materials: a law for strain gradient plasticity, Journal of the Mechanics and Physics of Solids **46**, 411 (1998).

[24] R. Bolin, H. Yavas, H. Song, K. J. Hemker, and S. Papanikolaou, Bending nanoindentation and plasticity noise in fcc single and polycrystals, Crystals **9**, 652 (2019).
[25] K. Durst, B. Backes, O. Franke, and M. Göken, Indentation size effect in metallic materials: Modeling strength from pop-in to macroscopic hardness using geometrically necessary dislocations, Acta Materialia **54**, 2547 (2006).
[26] S. Papanikolaou, Y. Cui, and N. Ghoniem, Avalanches and plastic flow in crystal plasticity: an overview, Modelling and Simulation in Materials Science and Engineering **26**, 013001 (2017).
[27] A. Ruiz-Moreno and P. Hähner, Indentation size effects of ferritic/martensitic steels: A comparative experimental and modelling study, Materials & Design **145**, 168 (2018).
[28] L. Kurpaska, F. Dominguez-Gutierrez, Y. Zhang, K. Mulewska, H. Bei, W. Weber, A. Kosińska, W. Chrominski, I. Jozwik, R. Alvarez-Donado, *et al.*, Effects of fe atoms on hardening of a nickel matrix: Nanoindentation experiments and atom-scale numerical modeling, Materials & Design **217**, 110639 (2022).
[29] A. Gouldstone, N. Chollacoop, M. Dao, J. Li, A. M. Minor, and Y.-L. Shen, Indentation across size scales and disciplines: Recent developments in experimentation and modeling, Acta Materialia **55**, 4015 (2007).
[30] S. Kossman and M. Bigerelle, Pop-in identification in nanoindentation curves with deep learning algorithms, Materials **14**, 7027 (2021).
[31] F. J. Domínguez-Gutíerrez, K. Mulewska, A. Ustrzycka, R. Alvarez-Donado, A. Kosínska, W. Huo, L. Kurpaska, I. Jozwik, S. Papanikolaou, and M. Alava, Mechanisms of strength and hardening in austenitic stainless 310s steel: Nanoindentation experiments and multiscale modeling, arXiv preprint arXiv:2205.03050 (2022).
[32] F. Bachmann, R. Hielscher, P. E. Jupp, W. Pantleon, H. Schaeben, and E. Wegert, Inferential statistics of electron backscatter diffraction data from within individual crystalline grains, Journal of Applied Crystallography **43**, 1338 (2010).
[33] W. C. Oliver and G. M. Pharr, An improved technique for determining hardness and elastic modulus using load and displacement sensing indentation experiments, Journal of materials research **7**, 1564 (1992).

APPENDIX

In this appendix, we present the actual and predicted load-depth curves associated with a subset of the indented grains within the testing sets in Fig. A1 and training sets in Fig. A2. The first and second rows indicate bottom 5% (good predictions) and top 5% (poor predictions) in mean-squared errors.

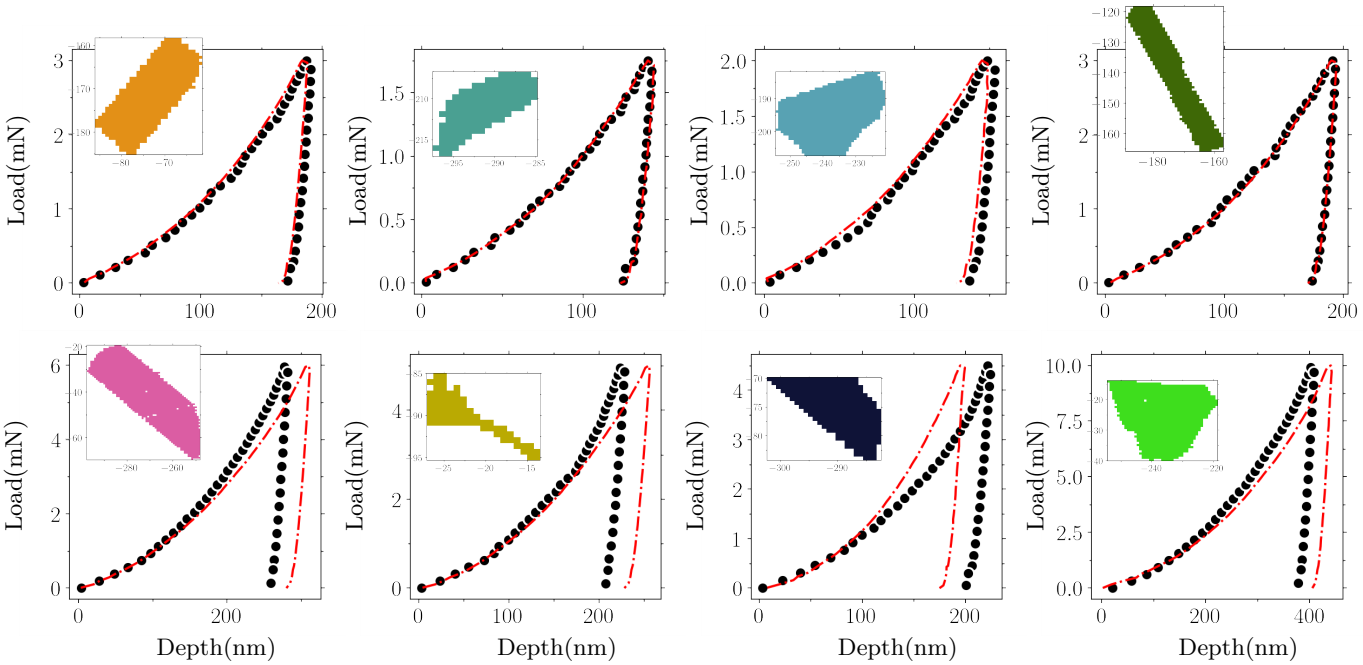

FIG. A1. Actual (symbols) and predicted (dashdotted curve) load-depth curves associated with a subset of the indented grains (the insets) within the test set. The first and second rows indicate bottom 5% (good predictions) and top 5% (poor predictions) in mean-squared errors.

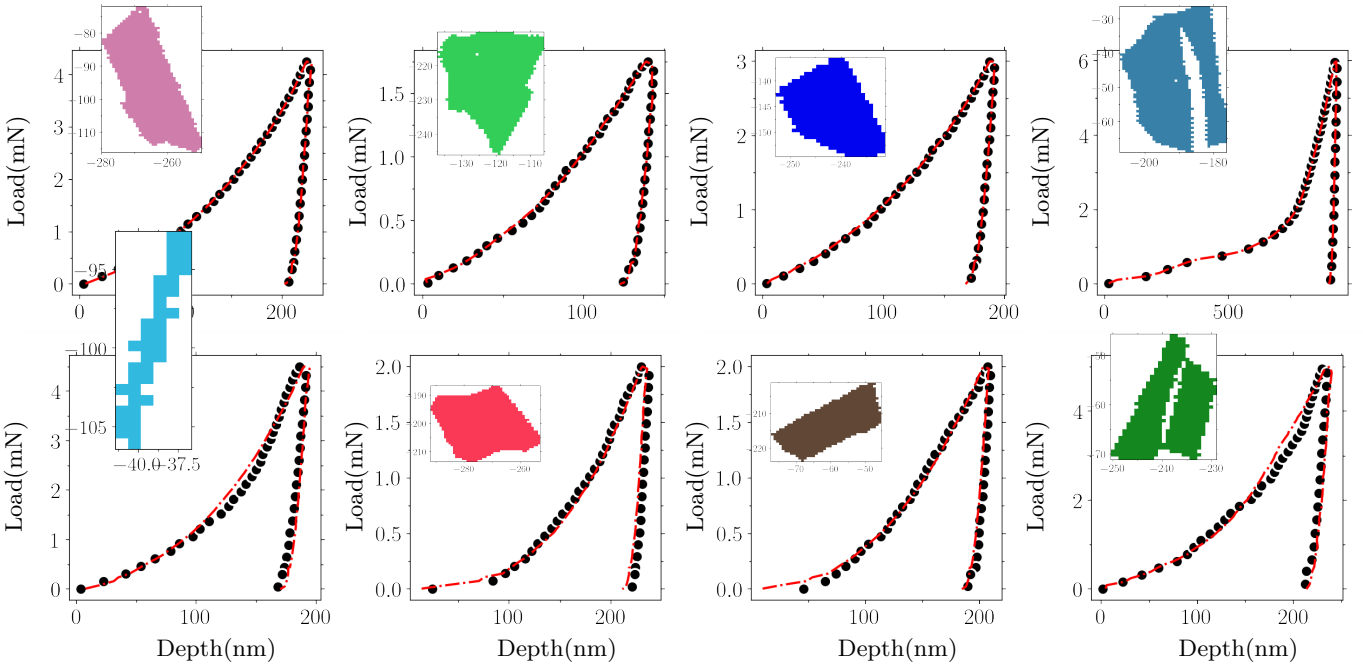

FIG. A2. Actual (symbols) and predicted (dashdotted curve) load-depth curves associated with a subset of the indented grains (insets) within the training sets. The first and second rows indicate bottom 5% (good predictions) and top 5% (poor predictions) in mean-squared errors.